

# Exact Frequency-Domain Reconstruction for Thermoacoustic Tomography—I: Planar Geometry

Yuan Xu, Dazi Feng, and Lihong V. Wang\*

**Abstract**—We report an exact and fast Fourier-domain reconstruction algorithm for thermoacoustic tomography in a planar configuration assuming thermal confinement and constant acoustic speed. The effects of the finite size of the detector and the finite length of the excitation pulse are explicitly included in the reconstruction algorithm. The algorithm is numerically and experimentally verified. We also demonstrate that the blurring caused by the finite size of the detector surface is the primary limiting factor on the resolution and that it can be compensated for by deconvolution.

**Index Terms**—Fourier-domain reconstruction, planar, thermoacoustic tomography.

## I. INTRODUCTION

USING thermoacoustic tomography (TAT) to image biological tissues has two primary advantages. The first is the high spatial resolution comparable with pure ultrasound imaging. The second advantage results from the large contrast in microwave absorption that exists between cancerous tissue and the normal tissue [1]–[7]. Reviews of TAT and related works [8]–[17] can be found in [11] and [18].

Various reconstruction algorithms for TAT [8], [9], [16], [18], [19] have been reported. Under the approximation that the distance between the detector and the absorbing object is much larger than the dimension of the absorbing object, a three-dimensional (3-D) Radon transform was applied to reconstruct the object in TAT [8]. However, the fact that this approximation may not always hold in real-world situations limits the application of this method. Further, the spatial resolutions of the imaging system using this reconstruction method are limited by blurs [20] caused by the finite size of the transducer surface, the finite width of the stimulating pulse, and the finite bandwidth of the transducers and amplifiers. Among these effects, the blur from the size of the transducer surface is expected to be the largest contributor to the total blur. The analysis of error is

limited in numerical simulations, and, hence, no analytical form was available prior to this work. A time-domain beam-forming technique was applied in one study to image reconstruction for the photoacoustic scanning of tissue structures [9]. A weighted delay-and-sum algorithm was used to account for the near-field effect and to reduce noise. This algorithm is an approximate one, and its lateral resolution is limited by the size of the detector surface. The above reconstructions were implemented in the time domain and consequently are time-consuming, especially in 3-D tomography. TAT was also obtained in a way similar to that used in conventional B-scan ultrasonic imaging, but it had difficulty detecting the boundaries of objects that are oblique to the transducer axis [16]. Exact reconstructions have been implemented for TAT in spherical and cylindrical configurations in the companion papers [18], [19].

Next, we present our studies on an exact and fast reconstruction algorithm using a Fourier transform for TAT in a planar configuration. The reconstruction of an image by Fourier transform has been used in X-ray computed tomography [21], ultrasonic reflectivity imaging [22]–[24], and diffraction tomography [25] successfully. The computation complexity is reduced greatly due to the efficiency of the Fourier transform. We developed image reconstruction by Fourier transform for planar TAT and obtained an exact reconstruction algorithm for the first time. Furthermore, some limitations from experiments, such as the effects of the finite size of the detectors and the finite length of the excitation pulse, are included explicitly in the reconstruction algorithm. The reconstruction algorithm is verified by both numerically simulated and experimental results. Our simulations also demonstrate that the blur due to the finite size of the detector surface, which is a key limiting factor on the resolution of images [9], [20], can be alleviated by deconvolution with respect to the size of the detector surface. Other effects that may cause blurring of images can be treated in a similar way. In our initial experiments, an image in good agreement with the real objects was reconstructed and the deconvolution improved the resolution of the imaging system.

## II. METHODS

### A. Image Reconstruction

Assume that the detector scans within the plane  $z = 0$  and that the object is distributed only in the half space  $z' > 0$ . In order to obtain a spatial resolution of about 1 mm, the microwave pulse should be set to less than  $\sim 1 \mu\text{s}$  because the speed of sound in soft biological tissue is  $\sim 1.5 \text{ mm}/\mu\text{s}$ . For these parameters, the diffusion term in the heat conduction equation is about six orders of magnitude less than the term of the

Manuscript received May 15, 2001; revised May 13, 2002. This work was supported in part by the U.S. Army Medical Research and Materiel Command under Grant DAMD17-00-1-0455, in part by the National Institutes of Health (NIH) under Grant R01 CA71980 and Grant R21 CA83760, in part by the National Science Foundation (NSF) under Grant BES-9734491, and in part by the Texas Higher Education Coordinating Board under Grant ARP 000512-0123-1999. The Associate Editor responsible for coordinating the review of this paper and recommending its publication was G. Wang. *Asterisk indicates corresponding author.*

Y. Xu and D. Feng are with the Optical Imaging Laboratory, Department of Biomedical Engineering, Texas A&M University, College Station, TX 77843-3120 USA.

\*L. V. Wang is with the Optical Imaging Laboratory, Department of Biomedical Engineering, Texas A&M University, 3120 TAMU, College Station, TX 77843-3120 USA (e-mail: LWang@tamu.edu).

Publisher Item Identifier 10.1109/TMI.2002.801172.

first-derivative of the temperature [26]. Therefore, heat conduction can be ignored. This is known as the assumption of thermal confinement. In this case, the acoustic wave  $p(\mathbf{r}, \bar{t})$  is related to microwave absorption  $H(\mathbf{r}, \bar{t})$  by the following wave equation [26]:

$$\frac{\partial^2 p(\mathbf{r}, \bar{t})}{\partial \bar{t}^2} - \nabla^2 p(\mathbf{r}, \bar{t}) = \frac{\beta v_s}{C} \frac{\partial H(\mathbf{r}, \bar{t})}{\partial \bar{t}} \quad (1)$$

where  $\bar{t} = tv_s$ ,  $v_s$  is the acoustic speed,  $C$  is the specific heat, and  $\beta$  is the coefficient of volume thermal expansion. In (1), the acoustic speed is assumed constant, which will be further addressed in the discussion section. Equation (1) can be rewritten in terms of  $H(\mathbf{r}', \bar{t})$ :

$$p(\mathbf{r}, \bar{t}) = \frac{\beta v_s}{4\pi C} \iiint \frac{\partial H(\mathbf{r}', t')}{\partial t'} \frac{d\mathbf{r}'}{|\mathbf{r} - \mathbf{r}'|} \quad (2)$$

where  $t' = \bar{t} - |\mathbf{r} - \mathbf{r}'|$ . The source term  $H(\mathbf{r}', \bar{t})$  can further be written as the product of a purely spatial and a purely temporal component, i.e.,

$$H(\mathbf{r}', \bar{t}) = I_0 \varphi(\mathbf{r}') \eta(\bar{t}) \quad (3)$$

where  $I_0$  is a scaling factor proportional to the incident radiation intensity,  $\varphi(\mathbf{r}')$  describes the microwave absorption properties of the medium at  $\mathbf{r}'$ .  $\eta(\bar{t})$  describes the shape of the irradiating pulse and is a nonnegative function whose integration over time equals the pulse energy. Substituting (3) into (2) results in

$$p(\mathbf{r}, \bar{t}) = \frac{I_0 \beta v_s}{4\pi C} \iiint \varphi(\mathbf{r}') \frac{d\eta(t')}{dt'} \frac{d\mathbf{r}'}{|\mathbf{r} - \mathbf{r}'|}. \quad (4)$$

We proceed by transforming the time-dependent wave equation into the temporal-frequency domain. Denoting the Fourier transforms of  $p$  and  $\eta$  by  $\bar{p}$  and  $\bar{\eta}$ , we have

$$p(\mathbf{r}, \bar{t}) = \int_{-\infty}^{\infty} \bar{p}(\mathbf{r}, k) \exp(ik\bar{t}) dk \quad (5)$$

$$\eta(\bar{t}) = \int_{-\infty}^{\infty} \bar{\eta}(k) \exp(ik\bar{t}) dk. \quad (6)$$

Substituting (5) and (6) into (4) results in

$$\bar{p}(\mathbf{r}, k) = \frac{i\beta v_s I_0 k \bar{\eta}(k)}{4\pi C} \iiint \varphi(\mathbf{r}') \frac{\exp(-ik|\mathbf{r} - \mathbf{r}'|)}{|\mathbf{r} - \mathbf{r}'|} d\mathbf{r}'. \quad (7)$$

If the acoustic signals are collected along a line or in a plane, for example at  $z = 0$ , following the line of Norton and Linzer in [22], it can be shown that for the case  $|k| > \rho$  and  $z' > 0$

$$\bar{P}(u, v, k) = \frac{\beta v_s I_0 k \bar{\eta}(k) \text{sgn}(k)}{2C \sqrt{k^2 - \rho^2}} \cdot \int_0^{\infty} \Phi(v, v, z') \exp\left(-iz' \text{sgn}(k) \sqrt{k^2 - \rho^2}\right) dz' \quad (8)$$

where  $\rho^2 = u^2 + v^2$ ,  $\text{sgn}(k)$  is the signum function

$$\bar{P}(u, v, k) = \frac{1}{(2\pi)^2} \iint \bar{p}(x, y, 0, k) \cdot \exp(-i(ux + vy)) dx dy \quad (9)$$

and

$$\Phi(u, v, z') = \frac{1}{(2\pi)^2} \iint \varphi(\mathbf{r}') \cdot \exp(-i(ux' + vy')) dx' dy'. \quad (10)$$

Equation (8) can further be simplified to

$$\bar{P}(u, v, k) = \frac{\pi \beta v_s I_0 k \bar{\eta}(k) \text{sgn}(k) \Phi_1\left(u, v, \text{sgn}(k) \sqrt{k^2 - \rho^2}\right)}{C \sqrt{k^2 - \rho^2}} \quad (11)$$

where

$$\Phi_1(u, v, w) = \frac{1}{2\pi} \int_{-\infty}^{\infty} \Phi(u, v, z') \exp(-iwz') dz'. \quad (12)$$

The lower limit of the above integration is changed from 0 to  $-\infty$  because  $\Phi(u, v, z') = 0$  when  $z' < 0$ . Equation (11) gives an exact mapping relation between the spectrum of the collected signals and the spectrum of the distribution of microwave energy deposition and is the essence of our reconstruction method. However, (11) stands only if the acoustic detector is a point detector. In practice, the detector is of finite size, whose surface shape can be described by  $R(x, y)$ . The signal from the detector  $p_d(x, y, t)$  can be expressed as an integral of the acoustic wave  $p(\mathbf{r}, t)$  over the detector surface

$$p_d(x, y, t) = \iint_s p(x', y', t) R(x' - x, y' - y) dx' dy'. \quad (13)$$

After transforming (13) into the temporal- and spatial-frequency domain, we have

$$\bar{P}_d(u, v, k) = 4\pi^2 \bar{P}(u, v, k) \bar{R}(-u, -v) \quad (14)$$

where  $\bar{P}_d(u, v, k)$  is the temporal and spatial Fourier transform of  $p_d(x, y, t)$ , and  $\bar{R}(u, v)$  is the spatial Fourier transform of  $R(x, y)$ . Substituting (14) into (11) results in

$$\bar{P}_d(u, v, k) = \frac{4\pi^3 \beta v_s I_0 k \bar{\eta}(k) \text{sgn}(k) \bar{R}(-u, -v) \Phi_1\left(u, v, \text{sgn}(k) \sqrt{k^2 - \rho^2}\right)}{C \sqrt{k^2 - \rho^2}}. \quad (15)$$

Mapping the  $(u, v, k)$  space into the  $(u, v, w)$  space by the relation

$$w = \text{sgn}(k) \sqrt{k^2 - \rho^2} \quad (16)$$

yields an explicit expression for  $\Phi_1$

$$\Phi_1(u, v, w) = \frac{C w \bar{P}_d\left(u, v, \text{sgn}(w) \sqrt{w^2 + \rho^2}\right)}{4\pi^3 \beta v_s I_0 \text{sgn}(w) \sqrt{w^2 + \rho^2} \bar{\eta}\left(\text{sgn}(w) \sqrt{w^2 + \rho^2}\right) \bar{R}(-u, -v)}. \quad (17)$$

At last, the distribution of the microwave energy deposition can be reconstructed from  $\Phi_1$  by 3-D inverse Fourier transform. Equation (17) gives an exact reconstruction algorithm for planar

TAT for the first time. Furthermore, the effects of the finite size of the detectors and the finite length of the excitation pulse are included explicitly. From (17), it can be inferred that the reconstructed image spectrum  $\Phi_d(u, v, w)$  from the experimental data without the consideration of these two effects, as was presented by previous researchers [9], [20], is related to the actual image spectrum  $\Phi_1(u, v, w)$  by

$$\begin{aligned} &\Phi_d(u, v, w) \\ &= 4\pi^2\eta \left( \text{sgn}(w)\sqrt{w^2 + \rho^2} \right) \bar{R}(-u, -v)\Phi_1(u, v, w). \end{aligned} \quad (18)$$

Both of the effects result in multiplications of a function to the actual image spectrum in the frequency domain. They are equivalent to convolutions in the spatial domain, which blur the reconstructed image. However, given the pulse shape and the surface configuration of the detector surface, the two effects can be reduced by deconvolution.

To summarize, the reconstruction procedure consists of the following steps.

- 1) The signal from the detector  $p_d(x, y, \bar{t})$  is Fourier transformed with respect to  $\bar{t}$  to yield  $\bar{p}_d(x, y, k)$ . Deconvolution with respect to the finite pulse length can be implemented immediately after the Fourier transform.
- 2)  $\bar{p}_d(x, y, k)$  is Fourier transformed with respect to  $x$  and  $y$ , yielding  $\bar{P}_d(u, v, k)$ .
- 3) According to (16) and (17),  $\bar{P}_d(u, v, k)$  is mapped to  $\Phi_d(u, v, w)$ .
- 4)  $\Phi_d(u, v, w)$  is deconvoluted with respect to the finite size of the detector, giving  $\Phi_1(u, v, w)$ .
- 5)  $\Phi_1(u, v, w)$  is inversely Fourier transformed with respect to  $u, v, w$  to yield  $\varphi(x', y', z')$ .

The order of steps 4) and 5) can be exchanged so that more stable deconvolution algorithms can be applied. In numerical calculations,  $\bar{P}_d(u, v, k)$  is obtained only at discrete points; hence the mapping from  $\bar{P}_d(u, v, k)$  to  $\Phi_d(u, v, w)$  needs interpolation, which can be a major source of distortion.

### B. System Setting

The experimental setup was reported in [27] and, for convenience, is only briefly described here (Fig. 1). The  $x$  axis points perpendicularly to the drawing plane; the  $y$  axis points to the right in the plane; and the  $z$  axis points downward along the acoustic axis. Microwave pulses are transmitted by a 9-GHz microwave generator. The pulse width is  $0.5 \mu\text{s}$ . The object to be imaged is a cylinder of pork fat containing a thin layer of connective tissue and six yellow microstructures. The diameter of the cylinder fat is 14 mm and the length in the  $x$  direction 30 mm. The cylinder was immersed in mineral oil in a plexi-glass tank. The central frequency of the ultrasonic transducer (Panametrics) is 2.25 MHz; the bandwidth 1.8 MHz; and the diameter of the active element 6 mm. More details about the system can be found in [27].

## III. RESULTS AND DISCUSSION

Our method was applied to reconstructing images from both the simulated and the experimental data in a two-dimensional (2-D) case, where the imaged objects were uniform along the  $x$

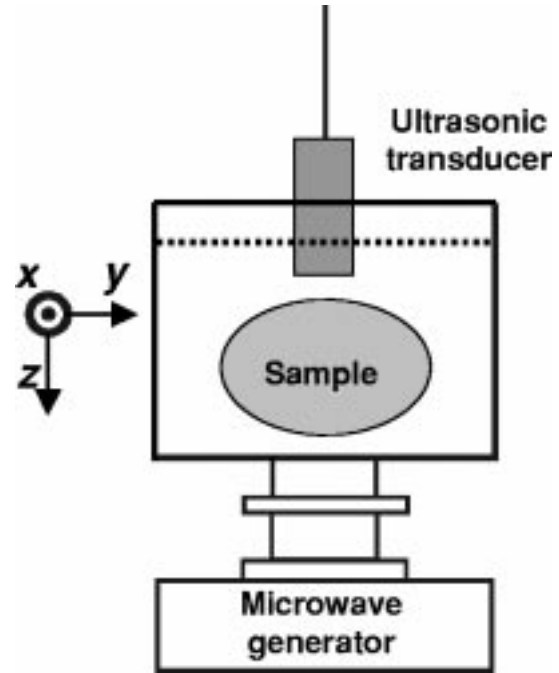


Fig. 1. Experimental setup for TAT.

axis. Because the blur due to the finite size of the detector surface is a limiting factor on the resolution of images, we demonstrated how deconvolution with respect to the detector surface can deblur the images. We chose the 2-D case here because both the computational and experimental complexity can be reduced more in the 2-D case than in the 3-D one. Nevertheless, the extension of the conclusions of the 2-D case to the 3-D one is straightforward.

### A. Simulation

The thermoacoustic imaging of two cylinders was numerically simulated. Cylinders were chosen because the analytical expression for their thermoacoustic signal is available [28]. In the simulations, the temporal-frequency range was from near 0 to 1.5 MHz, which was in accordance with the experimental one and with our previous experiments [11]. Two simulations were run. The first one was to test our reconstruction algorithm under an ideal experimental condition, which is noiseless and does not consider any experimental limitations on the detectors. In the second case, the effect of the finite size of the detectors on the imaging was studied while noise was also added. Deconvolution with respect to the finite size of the detector surface was applied to improve the lateral resolution of the blurred image. Since energy deposition is a positive value, only the positive components of the reconstructed image were retained, and the others were set to zero.

In step 3) of the reconstruction, which is the mapping from  $\bar{P}_d(u, v, k)$  to  $\Phi_d(u, v, w)$ , linear interpolation was applied. By adopting the zero-padding technique [25] for the time-domain data, one can increase the sampling density in the  $k$ -space and, consequently, obtain a better performance of the interpolation in the  $k$ -space. In the reconstruction from the simulation data and experimental data, we appended to the end of the data the same number of zeros as in the original collected data, so that

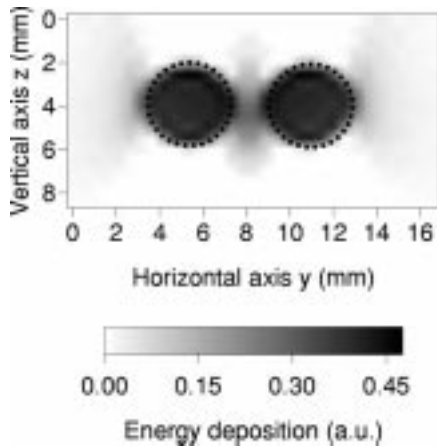


Fig. 2. The reconstructed image of the cross-section of two cylinders with a radius of 2 mm and the centers separated by 5.5 mm under ideal experimental conditions.

the sampling density in the  $k$ -space was doubled. By utilizing the Wiener filtering method [29], deconvolution with respect to the finite pulse length was implemented immediately after the Fourier transform with respect to time in step 1). As the deconvolution with respect to the finite size of the detector surface is much more unstable than the deconvolution with respect to the finite pulse length, we have tried two methods of deconvolution: the Wiener filtering method and the piecewise polynomial truncated singular value decomposition (PP-TSVD) [30] method. The first method can be implemented in the spatial-frequency domain and is more computationally efficient than the second, but the performance of the second method is much better, as it can restore sharp boundaries blurred by the convolution while avoiding the appearance of artificial oscillations in an unstable deconvolution. Therefore, we adopted the PP-TSVD method to process the images. Since the models in our simulation and experiment were uniform along the  $x$  axis, one-dimension deconvolution was applied.

Fig. 2 shows the reconstructed image from the simulated data under the ideal experimental condition, where the radius of the two cylinders was 2 mm; the distance between the centers of the cylinders was 5.5 mm; the centers of the cylinders were positioned in the plane of  $z = 10$  mm; the scanning range of the detector along the  $y$  axis was 90 mm with a step size of 0.5 mm; and the thermoacoustic signals were sampled for 40  $\mu$ s at a sampling rate of 50 MHz. The reconstructed image is in good agreement with the real objects, whose outlines are plotted as dotted circles in Fig. 2. The dimension of the cylinders is 3.75 mm along the  $z$  direction and 4.7 mm along the  $y$  direction. The cylinder is a little deformed laterally, which is due to the finite scanning range of the detector.

Fig. 3 shows the images before and after deconvolution with respect to the finite size of the detector surface in a case similar to our experimental conditions. The noise was added to the thermoacoustic signals, and the signal-to-noise ratio (SNR) was 50; the diameter of the detector was 6 mm. All of the other parameters were the same as those in the first case. The image before deconvolution is shown in Fig. 3(a). The dimension of the images of the objects is 3.5 mm along the  $y$  axis, which agrees well with the real one, 4 mm. However, along the  $z$  axis, the images

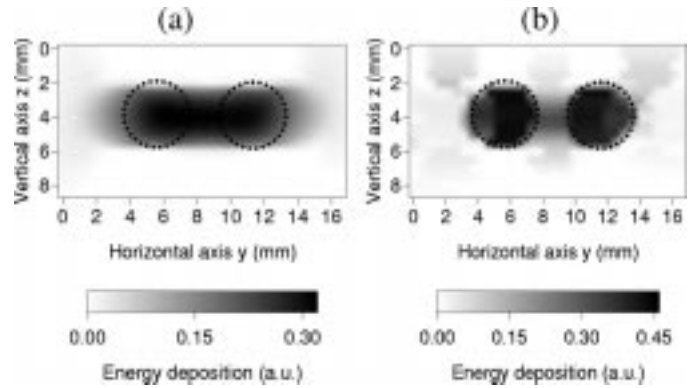


Fig. 3. The reconstructed images for the same two cylinders as in Fig. 2 from noisy data (a) before and (b) after the deconvolution with respect to the detector surface.

of the two cylinders were blurred and consequently merged into one, which is predicted by our analysis of the effect of the finite size of the detector. The image shows no clear boundaries of the objects along the  $y$  axis. After deconvolution, the lateral boundaries of the objects become very clear and the width of the objects in Fig. 3(b) is 4.1 mm, which is quite close to reality. Furthermore, the two objects can be distinguished clearly. After comparing Fig. 3(a) with (b), it seems that the ghost images become slightly more obvious, which is a disadvantage of deconvolution. Nevertheless, it is obvious that deconvolution with respect to the finite size of the detector surface can improve the lateral resolution greatly.

In Figs. 2 and 3, there are some ghost images. In principle, our reconstruction method is exact under the assumption of thermal confinement and constant acoustic speed. However, several factors may introduce distortions. First, as mentioned at the end of part Section II-A, the mapping from  $\bar{P}_d(u, v, k)$  to  $\Phi_d(u, v, w)$  needs interpolation, which is a major source of distortion. This distortion can be reduced by increasing sampling time or applying a better interpolation algorithm in the mapping. Second, in experiments, the detector cannot be scanned over the whole plane. Nevertheless, Fig. 2 shows that collecting data within a finite area of the collection plane can produce images of sufficient definition to determine the configuration and position of the objects.

### B. Experimental Result

Fig. 4 shows the experimental result. The images before and after deconvolution with respect to the finite size of the detector surface are shown in Fig. 4(a) and (b), respectively. Fig. 4(c) is the cross section of the biological tissue, which was a cylinder with a radius of about 14 mm and 3 cm long. It consisted of two parts of fat separated by a very thin layer of connective tissue, which is labeled as (7) in the middle of the sample. There were some yellow microstructures among the fat, labeled from (1)–(6), respectively. Fig. 4(a) is the image reconstructed from the experimental data before deconvolution. The connective tissue between the two parts of fat and the yellow microstructures are imaged clearly. The dimension of the image is 16.4 mm along the  $z$  direction and 19.2 mm along the  $y$  direction. However, it is obvious that the image before deconvolution is blurred along the  $y$  axis, which makes

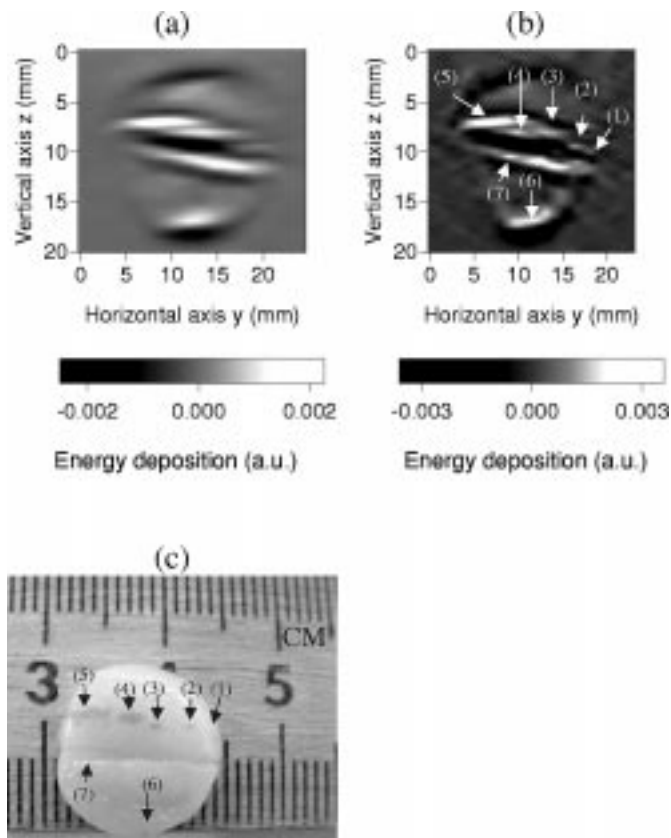


Fig. 4. The reconstructed images from the experimental data (a) before and (b) after the deconvolution with respect to the detector surface; (c) the cross section of a cylinder of fat sample containing six yellow microstructures labeled from (1)–(6) and a layer of connective tissue in the middle labeled as (7).

the lateral boundaries unclear and the yellow microstructures (1) and (2), (3) and (4) merge into one object, respectively. The lateral resolution of the image needs to be improved. Consequently, deconvolution with respect to the finite size of the detector surface was applied to Fig. 4(a), and the result is shown in Fig. 4(b). The lateral resolution of the image after deconvolution is much improved. The merged objects can be distinguished clearly, and the lateral boundaries of the cylinder become much clearer. The dimension of the image is 16.4 mm along the  $z$  direction and 16.7 mm along the  $y$  direction.

### C. Discussion

There are several advantages of our reconstruction method. The first one is that it is an exact reconstruction algorithm. Unlike other reconstruction methods for TAT that are approximate ones, our reconstruction method provides a solid base for analyzing and improving the quality of reconstructed images. Furthermore, the exact reconstruction method has a broader application than the approximate ones. For example, in both our simulation and experiment, the closest distance between the objects and the detectors was only about 1 cm; this is possible because in principle there is no limitation on the detector–object distance in our method. In other words, the detector can be placed very close to the object to ensure a better SNR. The second advantage of our method is that it can explicitly include the effect of many limitations from the experiment, such as the finite size of detector surface, the microwave pulse

length, and the finite frequency response range of the detector. Actually, these analyses are also valid for other approximate reconstruction methods as long as the other reconstruction methods are able to produce images approximating the real objects. Consequently, our analysis of the blur caused by the various experimental limitations can also be very useful for eliminating the limitations in other reconstruction methods. Lastly, since the reconstruction in our method is implemented in the frequency domain, the efficiency of computation is much better than the algorithm implemented in the time domain due to the use of the efficient Fourier transformation in our method. This is especially important for real-time 3-D imaging.

From the above images, it can be seen that there is no speckle in the reconstructed image. Speckles are an important factor limiting the quality of pure ultrasonic imaging. In our technology, the detected signals are directly from the primary acoustic waves rather than reflective or scattered waves. Further, the temporal frequency of the acoustic signals lies in a range from 0 to 1.5 MHz, which is only weakly scattered in the tissues. The above two factors guarantee that there is no obvious speckle in our experimental images. However, the issue of image speckle in more realistic medical imaging applications of our algorithm is a topic for future consideration.

The formulas in this paper are for TAT in planar geometry only. However, for cylindrical geometry [19], we can predict that the lateral resolution of images can also be improved by deconvolution with respect to the detector surface, where the deconvolution is carried out in a cylindrical surface instead of a plane. For spherical geometry [18], similar work can be conducted as well.

For many medical imaging applications, the acoustic speed may not be constant. For example, the acoustic speed inside the female breast may typically exhibit a 10% variation; however, our simulation, to be reported elsewhere, showed that the image distortion is relatively small.

## IV. CONCLUSION

We developed a Fourier-domain reconstruction for TAT and obtained an exact and fast reconstruction algorithm. The effects of the finite size of the detectors and the finite length of the excitation pulse were included explicitly in the reconstruction algorithm. The reconstruction algorithm was verified by both numerical simulations and experimental results. Our simulations demonstrated that the blurring caused by the finite size of the detector surface, which is a key limiting factor on the resolution of images, can be alleviated by deconvolution with respect to the detector surface. Other effects that may cause the blur of the images can be treated in a similar way. In the initial experiment, an image in good agreement with the real objects was reconstructed and the deconvolution improved the resolution of the imaging system. The method can also be extended to other configurations of data collection.

## REFERENCES

- [1] W. Joines, R. Jirtle, M. Rafal, and D. Schaeffer, "Microwave power absorption differences between normal and malignant tissue," *Radiation Oncol. Biol. Phys.*, vol. 6, pp. 681–687, 1980.

- [2] S. Chaudhary, R. Mishra, A. Swarup, and J. Thomas, "Dielectric properties of normal human breast tissues at radiowave and microwave frequencies," *Indian J. Biochem. Biophys.*, vol. 21, pp. 76–79, 1984.
- [3] W. Joines, Y. Zhang, C. Li, and R. Jirtle, "The measured electrical properties of normal and malignant human tissues from 50–900 MHz," *Med. Phys.*, vol. 21, pp. 547–550, 1994.
- [4] L. E. Larsen and J. H. Jacobi, Eds., *Medical Applications of Microwave Imaging*. Piscataway, NJ: IEEE Press, 1986.
- [5] S. Caorsi, A. Frattoni, G. L. Gragnani, E. Nortino, and M. Pastorino, "Numerical algorithm for dielectric-permittivity microwave imaging of inhomogeneous biological bodies," *Med. Biol. Eng. Comput.*, vol. NS-29, pp. 37–44, 1991.
- [6] M. S. Hawley, A. Broquetas, L. Jofre, J. C. Bolomey, and G. Gaboriaud, "Microwave imaging of tissue blood content changes," *J. Biomed. Eng.*, vol. 13, pp. 197–202, 1991.
- [7] P. M. Meaney, K. D. Paulsen, and J. T. Chang, "Near-field microwave imaging of biologically-based materials using a monopole transceiver system," *IEEE Trans. Microwave Theory Tech.*, vol. 46, pp. 31–45, Jan 1998.
- [8] R. A. Kruger, P. Liu, Y. R. Fang, and C. R. Appledorn, "Photoacoustic ultrasound (PAUS)—Reconstruction tomography," *Med. Phys.*, vol. 22, pp. 1605–1609, 1995.
- [9] C. G. A. Hoelen, F. F. M. Demul, R. Pongers, and A. Dekker, "Three-dimensional photoacoustic imaging of blood vessels in tissue," *Opt. Lett.*, vol. 23, pp. 648–650, 1998.
- [10] A. A. Karabutov, E. V. Savateeva, N. B. Podymova, and A. A. Oraevsky, "Backward mode detection of laser-induced wide-band ultrasonic transients with optoacoustic transducer," *J. Appl. Phys.*, vol. 87, pp. 2003–2014, 2000.
- [11] Y. Xu and L.-H. V. Wang, "Signal processing in scanning thermoacoustic tomography in biological tissues," *Med. Phys.*, vol. 28, pp. 1519–1524, 2001.
- [12] T. Bowen, L. Nasoni, A. E. Pifer, and G. H. Sembrosk, "Some experimental results on the thermoacoustic imaging of soft tissue-equivalent phantoms," in *Proc. IEEE Ultrasonics Symp.*, vol. 2, 1981, pp. 823–827.
- [13] J. C. Lin and K. H. Chan, "Microwave thermoelastic tissue imaging—System design," *IEEE Trans. Microwave Theory Tech.*, vol. MTT-32, pp. 854–860, 1984.
- [14] R. A. Kruger, D. R. Reinecke, and G. A. Kruger, "—Thermoacoustic computed tomography Technical considerations," *Med. Phys.*, vol. 26, pp. 1832–1837, 1999.
- [15] L.-H. V. Wang, X. Zhao, H. Sun, and G. Ku, "Microwave-induced acoustic imaging of biological tissues," *Rev. Sci. Instrum.*, vol. 70, pp. 3744–3748, 1999.
- [16] G. Ku and L.-H. V. Wang, "Scanning thermoacoustic tomography in biological tissue," *Med. Phys.*, vol. 27, pp. 1195–1202, 2000.
- [17] —, "Scanning microwave-induced thermoacoustic tomography: Signal, resolution, and contrast," *Med. Phys.*, vol. 28, pp. 4–10, 2001.
- [18] M. Xu and L.-H. V. Wang, "Time-domain reconstruction for thermoacoustic tomography in a spherical geometry," *IEEE Trans. Med. Imag.*, vol. 21, pp. 814–822, July 2002.
- [19] Y. Xu, M. Xu, and L.-H. V. Wang, "Exact frequency-domain reconstruction for thermoacoustic tomography—II: Cylindrical geometry," *IEEE Trans. Med. Imag.*, vol. 21, pp. 829–833, July 2002.
- [20] W. J. Kiser, Jr. and R. A. Kruger, "Thermoacoustic computed tomography—limits to spatial resolution," *SPIE*, vol. 3659, pp. 895–905, 1999.
- [21] H. Stark, J. W. Woods, I. Paul, and R. Hingoram, "Direct Fourier reconstruction in computer tomography," *IEEE Trans. Acoust. Speech Signal Processing*, vol. ASSP-29, pp. 237–245, 1981.
- [22] S. J. Norton and M. Linzer, "Ultrasonic reflectivity imaging in three dimensions: Exact inverse scattering solution for plane, cylindrical and spherical aperture," *IEEE Trans. Biomed. Eng.*, vol. BME-28, pp. 202–220, Feb. 1981.
- [23] K. Nagai, "A new synthetic-aperture focusing method for ultrasonic b-scan imaging by the Fourier transform," *IEEE Trans. Sonics Ultrason.*, vol. SU-32, pp. 531–536, 1985.
- [24] J. Lu, "Experimental study of high frame rate imaging with limited diffraction beams," *IEEE Trans. Ultrason. Ferroel. Frequency Control*, vol. 45, pp. 84–97, Jan. 1998.
- [25] S. X. Pan and A. C. Kak, "A computational study of reconstruction algorithms for diffraction tomography: Interpolation versus filtered backprojection," *IEEE Trans. Acoust. Speech Signal Processing*, vol. ASSP-31, pp. 1262–1275, 1983.
- [26] V. E. Gusev and A. A. Karabutov, *Laser Optoacoustics*. New York: Amer. Inst. Phys., 1993.
- [27] D. Feng, Y. Xu, G. Ku, and L.-H. V. Wang, "Microwave-induced thermoacoustic tomography: Reconstruction by synthetic aperture," *Med. Phys.*, vol. 28, pp. 2427–2431, 2001.
- [28] G. J. Diebold, M. I. Khan, and S. M. Park, "Photoacoustic signatures of particulate matter: Optical production of acoustic monopole radiation," *Science*, vol. 250, pp. 101–104, 1990.
- [29] A. K. Jain, *Fundamentals of Digital Image Processing*. Englewood Cliffs, NJ: Prentice Hall, 1989.
- [30] P. C. Hansen and K. Mosegaard, "Piecewise polynomial solutions without *priori* breakpoints," *Num. Lin. Alg. Applicat.*, vol. 3, pp. 513–524, 1996.